Detailed Theoretical and Experimental Study on a Large MHD Generator

J. F. Louis,* G. Gal,† AND P. R. Blackburn‡

Avco Corporation, Everett, Mass.

The paper describes the results of experiments on a large-size combustion-driven magneto-hydrodynamics (MHD) generator at magnetic field up to 3.3 weber/m², and mass flows up to 6.5 lb/sec. With large Reynolds number and magnetic field, the MHD phenomena dominate the flow and can be studied in great detail over a wide range of operating conditions. By a systematic study of the data obtained, the magnitude of the different losses can be determined accurately. Also, such phenomena as the location of the shock, the length of the separation region behind strong shocks, and electrode losses caused by the Hall field are studied. The theory used to describe the performance is largely one-dimensional and leads to detailed agreement with the experimental results.

Introduction

RESULTS of experiments carried out in a large MHD generator have been reported previously.[1] This paper describes further results, which led to a good understanding of MHD phenomena over a wide range of operating conditions and examines the detailed agreement between theory and experiments.

Section I describes the spectrum of experiments conducted on a modified channel having an area ratio of 2.5. The mass flows, Hall coefficient, the number, and width of electrodes were changed systematically to determine the parameters influencing the performance of the generator.

The method of theoretical analysis, largely one-dimensional, has been reported before[1] and is described briefly in Sec. II. The drag and heat-transfer coefficients were measured, the gas properties were determined theoretically, and the conductivity and Hall coefficients were calculated and verified experimentally. The electrode drop is also considered and has two components. The first is associated with the joule losses encountered by the current passage through the aerodynamic boundary layer and the second with Hall losses associated with the electrical boundary layer.

In Sec. III, the internal aerodynamics of the generator as influenced by MHD effects are analyzed under widely different flow conditions. The aerodynamic coefficients of friction and heat transfer previously determined[1] were confirmed by more experimental data on the Mark II and on smaller channels tested at Avco-Everett Research Laboratory. For supersonic flows and heavy loading, a shock can be formed. In this section, the location of the shock, its strength as influenced by boundary-layer separation, and the length of the separated region are studied. Because of the

large Lorenz force exerted on the gas, the shock location can be determined with reasonable accuracy.

Section IV studies the effects of the electrical boundary layers. On the highly cooled insulating walls, the conductivity vanishes in the inner boundary layer, and the Hartmann effect is negligible. The electrode, on the other hand, will operate at a temperature close to the gas temperature. The gas conductivity is finite, and the Hall field is shorted locally by the electrodes. The shorting of the Hall field at the surface of the electrodes occurs in an electrical boundary layer and produces losses, which depend upon $\omega\tau$ and the electrode geometry. These effects are studied in detail.

Section V compares the over-all performance determined from the detailed analysis with the relevant generator data. The good agreement found demonstrates the feasibility of predicting MHD generator performance, which is associated with a detailed understanding of the flow.

I.   Experimental Results

The experimental data were obtained in a channel 1.5 m long with inlet and outlet areas of 0.016 m² and 0.040 m², respectively. This channel was designed for a mass flow of 6 lb/sec, 33,000 gauss, and a flow velocity close to sonic. The working fluid was the combustion products of oxygen and a solution of 50% methylcyclohexane with 50% ethyl alcohol. Seeding was provided by potassium hydroxide, which was dissolved in the latter. The magnetic field was 33,000 gauss, and the mass flow was from 3 to 6.5 lb/sec.

Figure 1 describes the spectrum of experiments covered in this study. The mass flow varies from 6.5 to 3 lb/sec, together with drop in performance from 1500 to 200 kw. At mass flows larger than 5 lb/sec, the flow velocity is high, and
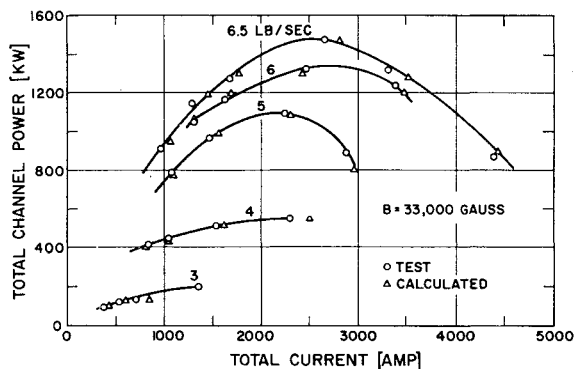

Fig. 1   Mark II B over-all performance at 33,000 gauss.

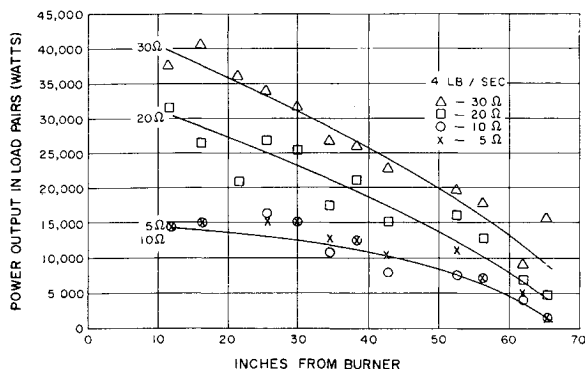**Fig. 2   Output power distribution at 4lb/sec and 33,000 gauss.**

Fig. 4   Hall field vs axial distance at 3 lb/sec and 33,000 gauss.

the isentropic efficiency reaches values up to 45%. At lower mass flows, the combined effects of large channel area ratio and high interaction makes the flow diffuse. The associated velocity drop results in reduced induced voltage and a subsequent power reduction. Figure 2 gives the output power distribution as a function of distance at 4 lb/sec and indicates the power drop associated with velocity reduction. The loading refers to the identical load seen by each pair of 50 segmented electrodes. Current and voltage were read at every fourth electrode with d.c. voltmeters and amperemeters. The power is calculated by multiplying the readings of current and voltage obtained at the time 8 sec, counted from the firing of the combustion chamber.

At open circuit, a voltage fluctuation was found on the oscilloscope trace. The measured amplitude of this fluctuation was a few percent of the total output, and its main frequency was around 5000 cps, which corresponds to a modulation induced by the acoustic waves tuned to the width of the channel. As the generator was loaded, this fluctuation rapidly disappeared in the noise of 400 cps and larger. The d.c. meters did not respond to these high-frequency modulations and were steady.

Figure 3 shows a very flat power distribution; the small drop toward the end for 10 and 20 Ω results from increasing electrode losses associated with large Hall coefficients. These losses are analyzed in the last section. Figure 4 gives the variation of the Hall field as a function of load and distance at low mass flow. It shows an increase of this field with the reduction in the resistance of the load as expected.

For given axial location and load condition, the velocity increases, and output voltage increases with the mass flow. Figure 5 describes the increase of output voltage as a function of mass flow. These voltage characteristics will have a direct bearing on the control of MHD generators. Further, the
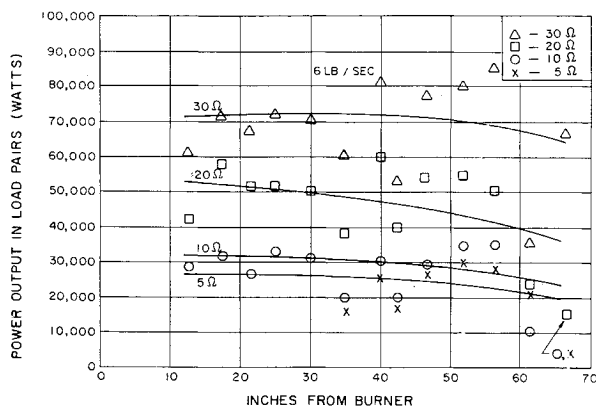
operation at low mass flow indicates that most of the interaction occurs in a length appreciably smaller than the generator length. The rest of the generator contributes little to the power output, and its drag on the flow is detrimental to the performance of the more active section. Figure 6 illustrates this point as it compares the performance of an older channel of 1.5 area ratio operating with 100 and 50% of the electrodes connected to the loads for given mass flows and magnetic field strength. It can be seen that the maximum power output is only reduced by 33% when the generator operates with only 50% of the electrodes.

II.   Theoretical Analysis

Because the MHD generator is an apparatus of a large length to hydraulic diameter ratio, the flow can be described

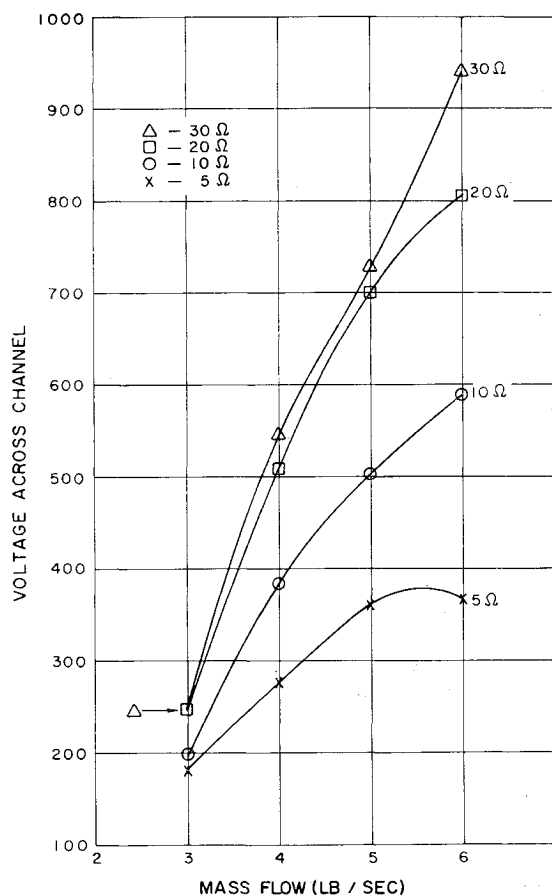**Fig. 3   Output power distribution at 6 lb/sec and 33,000 gauss.**

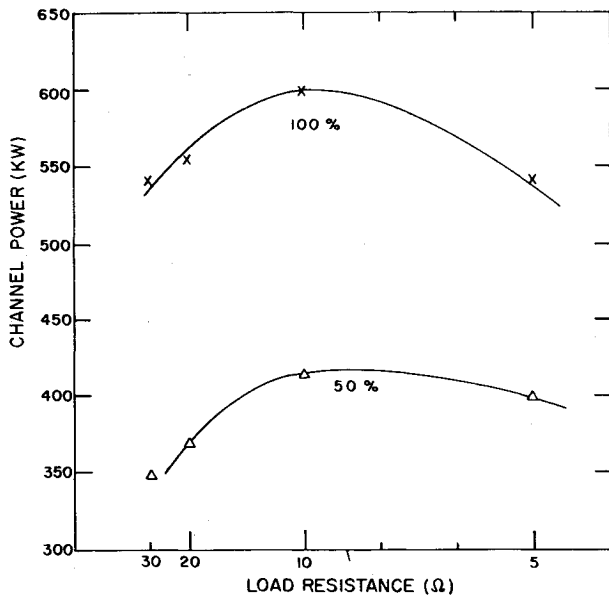**Fig. 5   Output voltage at midchannel vs mass flow.**

Fig. 6 Comparison of channel over-all performance with 100 and 50% of the electrodes connected.

by a quasi-one-dimensional analysis.[1] The analysis integrates the equations of energy, momentum, and continuity simultaneously along the axis of the machine. The equation of momentum includes the Lorenz force as a friction effect; the end losses or losses associated with the circulation of current are introduced as a stagnation-pressure loss. The equation of energy includes the heat transfer to the walls and electrical power output. The electrode drop is introduced as a drop in voltage output and appears as the reduced electrical power output. The real-gas properties, as calculated,[4] are used in this analysis. Similarly, the conductivity and Hall coefficients have been calculated and corrected for the discrepancy measured.[1] The equations used are:

Momentum

$$\frac{dp}{p} + \gamma \frac{M^2}{2}\left(\frac{dM^2}{M^2} + \frac{dT}{T} + \frac{dR}{R}\right) = \frac{-\gamma M^2}{2}\left\{\frac{4C_f}{D} + \right.$$

$$\left. \frac{2BA}{G}\left(\frac{\sigma\sigma_L}{\sigma + \sigma_L}\right) \times \left[B - \frac{E_{el}}{M(\gamma RT)^{1/2}}\right]\right\} dx + \frac{dp_0}{p} \quad (1)$$

Energy

$$\frac{Cp}{R}\frac{dT}{T} + \left[\rho\left(\frac{\partial h}{\partial p}\right)_T\right]\frac{dp}{p} + \frac{\gamma M^2}{2}\left[\frac{dM^2}{M^2} + \frac{dT}{T} + \frac{dR}{R}\right] =$$

$$-\left\{\frac{\sigma[BM(\gamma RT)^{1/2} - E_{el}]}{\sigma + \sigma_L}\right\} \cdot \left[\frac{\sigma\sigma_L}{\sigma + \sigma_L}\left(\frac{B}{P} - \right.\right.$$

$$\left.\left.\frac{A}{GRT}E_{el}\right)\right] dx - \left[\frac{C_H}{D}\frac{ho}{RT(Gx/A_\mu)^{0.2}}\right] dx \quad (2)$$

Continuity

$$\frac{1}{p}\frac{dp}{dx} - \frac{1}{2T}\frac{dT}{dx} + \frac{1}{2M^2}\frac{dM^2}{dx} - \frac{1}{2R}\frac{dR}{dx} + \frac{1}{A}\frac{dA}{dx} = 0 \quad (3)$$

with x = the axial distance, p = static pressure, M = Mach number, D = hydraulic diameter, T = temperature, C_f = friction coefficient, A = channel area, h = enthalpy, $h0$ = stagnation enthalpy, $\gamma = (\partial \ln p/\partial \ln \rho)_s$,§ B = magnetic field strength, ρ = gas density, G = mass flow, G_H = heat-

§ As pointed out by one referee, the local sonic velocity will differ slightly from $(\gamma RT)^{1/2}$ where γ is defined as $(\partial \ln p/\partial \ln \rho)_s$, since propagation of a sound wave involves essentially fixed composition changes rather than changes at equilibrium composition. $M = u/(\gamma RT)^{1/2}$ can be considered as a convenient definition needed to nondimensionalize the equations.

transfer coefficient, $\sigma_L = h/r_L$, LS is the equivalent load conductivity where h and L are the height and width of the channel, respectively, S = the electrode pitch, r_L = the external load, and E_{el} = the electrode drop. The latter will include the components due to the joule losses encountered in the aerodynamic boundary layer and the losses associated with the finite length of the electrodes and dp_0, the pressure loss function determined by the end losses and eddy currents due to the nonuniformities in the axial directions determined below.

The magnitude of circulating eddy currents can be related to curl $\bar{j}$. If the magnitude of the resultant eddy current is small with respect to the quantities producing it, the equations can be linearized and solved, using a perturbation theory. One writes

$$\bar{J} = J_y\bar{l}_y + \bar{j}$$

where $\bar{j}$ represents the eddy current flowing, and J_y is the current density determined in the one-dimensional theory. Ohm's law can be written with Hall effects as

$$\bar{J} = \sigma[\bar{E} + (\bar{U} \times \bar{B})] - (\omega\tau/B)(\bar{J} \times \bar{B})$$

with the preceding assumptions and neglecting second-order term

$$\text{curl}\,\bar{j} = -\frac{\partial J_y}{\partial x} + E_y\frac{\partial \sigma}{\partial x} + \frac{\partial}{\partial x}\sigma UB$$

As div$\bar{j}$ = 0, a function ϕ exists such that

$$j_x = -\partial\phi/\partial y \qquad \text{and} \qquad j_y = \partial\phi/\partial x$$

can be defined. The problem reduces to solving the Poisson equation

$$\nabla^2\phi = -\frac{\partial J_y}{\partial x} + E_y\frac{\partial \sigma}{\partial x} + \frac{\partial}{\partial x}\sigma UB$$

J_y, E_{y1}, σ, $U = M(\gamma RT)^{1/2}$, and B are known functions of x once the preceding analysis is carried out.

A solution for this equation $\Delta^2\phi = F(x)$ has been given[5] for a problem with the same boundary equations. Using this solution, j is determined, and the stagnation-pressure loss associated with the eddy current

$$\rho URTd\,\ln p_0 = \bar{j}^2/\sigma$$

A first analysis is carried out, assuming $dp_0 = 0$, through a rapidly converging iteration, and dp_0 and the flow are calculated.

For the analysis, the experimental conditions of mass flow, upstream stagnation temperature and pressure, magnetic field, load condition, and channel geometry are given. The preceding equations are integrated as a function of axial distance. The blockage caused by the growth of the boundary layer is also taken into account.[1]
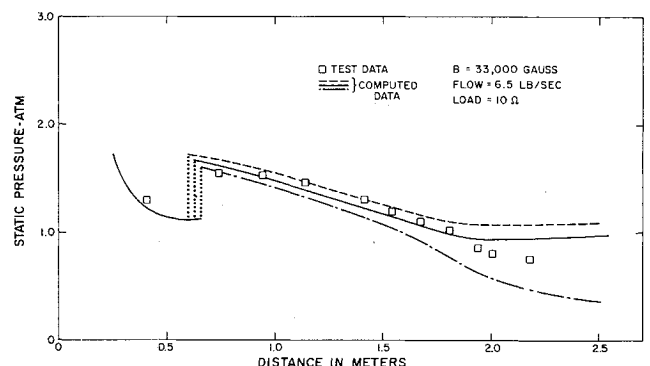

Fig. 7 Matching of the shock location with the downstream atmospheric pressure.

III. MHD Generator Internal Aerodynamics

The results[1] were confirmed in the results obtained in the work described herein. However, in the present work, much more experience and understanding was developed with MHD supersonic flows.

Supersonic flows are of interest in MHD generators because the power output is proportional to the conductivity and the square of the flow velocity. Therefore, gains in output power and efficiency can be envisaged by making use of supersonic flows. However, the reduction in conductivity and the increased friction effects associated with supersonic flows limit the range of power gain per unit volume to a Mach number of 1.4[¶] for the conditions of the present experiment.

MHD channel flow with supersonic flow throughout the channel can be accomplished by matching the mass flow, the duct geometry, and the loading. However, a mismatch because of a larger interaction requires a deceleration of the flow to subsonic velocities. In a stable channel flow, deceleration through the speed of sound can be accomplished only through a shock wave.[6] MHD flows with a shock wave present require the understanding of the following problems: 1) the determination of the shock location, 2) the determination of the shock strength as affected by the separated boundary layers at the shock location, and 3) the determination of the length of the separated region as influenced by the rate of velocity recovery and the magnitude of the Lorenz force.

A. Shock Location

In conventional channel flow, the friction force causes the existence of the shock, and the small magnitude of the friction force compared to the dynamic force results in an appreciable uncertainty in the shock location. In MHD channel flows, where the Lorenz force can be comparable to the dynamic force, the shock location can be obtained more accurately. The program described in Sec. II shows a distinct singularity at the point where the flow chokes. The shock steepening is indicated by a rapid change of the derivatives of the thermodynamic variables, and the rate of change is a function of the Lorenz force. Just ahead of this region, the static pressure passes through a minimum. Comparison between the theory and the experimental data indicates that the shock location can be taken at the point of minimum static pressure as a first approximation in the iteration process used to match the boundary condition, which is the downstream atmospheric pressure. Figure 7 shows the iteration process used to locate the shock by matching the downstream boundary condition. By locating the shock at the
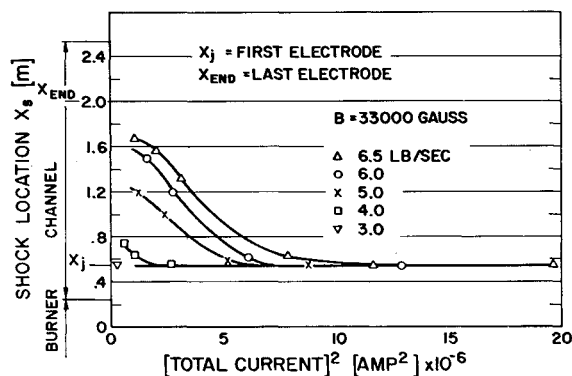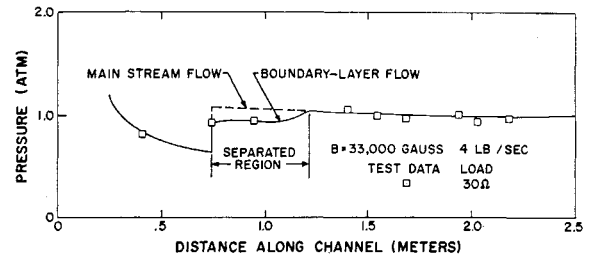

Fig. 9   Axial pressure distribution showing boundary separation behind the shock (experimental and calculated data).

point of minimum pressure (0.6 m), there is a slight positive mismatch of pressure downstream, whereas by moving the shock of 0.66 m, there is a negative mismatch. Finally, a shock location at 0.63 m shows a satisfactory match of the boundary condition and of the experimental data points. The existence of a shock is indicated experimentally by a sharp increase in static pressure and by a rapid variation of output voltage. Figure 8 shows the variation of the shock location for different mass flows and load factors as calculated and determined from the experiments.

B. Shock Strength

Although the supersonic Mach numbers encountered in the generator were relatively low (up to $M = 1.5$), the shocks present in the channel did interact with the relatively thick turbulent boundary layer. Many cases of boundary layer separation were observed.

In a conventional flow, a feedback exists between the shock and the boundary layer. The pressure rise causing separation is produced by the shock, and the latter is generated by the flow deflection associated with the flow separation. In a MHD flow, a second feedback exists between the upstream and the downstream of the shock because of the circulation of eddy currents. The sharp variation of velocity across the shock results in a difference of induced emf on both sides of the shock. This difference of emf will drive eddy currents across the shock. The strength and joule dissipation associated with this circulation can be calculated.[5]

Another departure from conventional supersonic flows is the different behavior of the boundary layers on the insulating and electrode walls that might lead to the occurrence of separation on certain walls preferentially. The boundary layer on the insulating wall is highly cooled as the walls are kept at temperatures below 500°C. The boundary layer is thin, and only the outer part of the layer is conductive. The variation of velocity in the outer part of the layer will result in a gradient of induced emf that will drive eddy currents. These will tend to accelerate the low velocity fluid. Therefore, the high cooling rate and MHD effects will tend to delay or reduce separation on the insulating walls.

On the other hand, the temperature of the electrodes is close to the temperature of the gas. The current induced by the mainstream passes through the boundary layer into the electrodes. The Lorenz force acting on the inner boundary layer will slow down the low momentum flow or accelerate it in the upstream direction. Therefore, the Lorenz force acting at the surface of the electrode walls can induce a separation or increase the recirculation within the separated boundary layer. This argument suggests that separation effects will be much stronger on the electrode wall than on the insulating wall. The evidence of separated boundary layer was given by the typical pressure distribution (Fig. 9) and the voltage distribution (Fig. 10), which indicates an extensive region of low velocity covering the cathode. The experiments indicate that separation is likely to occur when the Mach number immediately upstream of the shock is larger than 1.25.

Fig. 8   Variation of the shock location for different mass flows.

[¶] One referee mentioned that General Electric Report R-62-SD-990 arrived at the same conclusions concerning the optimum Mach number.
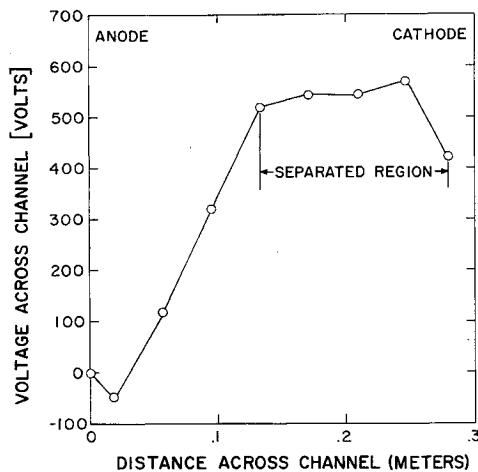
Fig. 10 Voltage distribution across channel indicating the existence of a separated boundary layer over the cathode wall.

The interaction between separated boundary layers and shock waves without MHD effects has been studied by many authors,[7,8] and some have derived the semiempirical formula

$$M_2{}^2 = CM_1{}^2 \qquad (4)$$

where M_1 and M_2 are the Mach numbers ahead of and behind the oblique shock induced by the separation, and C is a constant, which depends upon the type of velocity distribution existing in the separated boundary layer. Whereas theory[7] and data[8] indicate a value of $0.45 \leq C \leq 0.60$, our data yield a value of 0.64 ± 0.05.

For flows with shocks occurring at a Mach number less than 1.25, the Rankine-Hugoniot relationship is used. For flows with a shock occurring at a Mach number larger than 1.25, the previous relation between Mach number together with the conservation of energy and mass define the shock strength. However, the calculation of the flow behind the shock requires a calculation of the separated boundary layer to determine the blockage. Such calculations were attempted with some success. Figure 9 shows the pressure distribution obtained in the separated region that agrees with the experimental data. However, this calculation is lengthy and empirical as a velocity profile for the separated region has
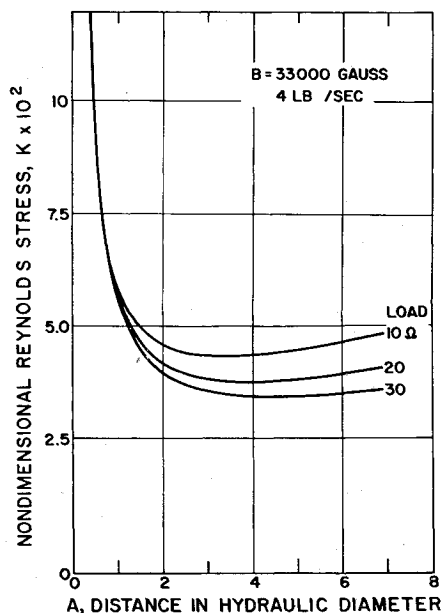

Fig. 11 Reynolds stress vs length.

to be assumed. Similar difficulty has been encountered previously in the flow studies of supersonic diffusers, and a diffuser efficiency is often defined; it takes into account the shock losses and the friction losses in a gross way. The data analysis showed that for shocks in the range $M = 1.30$ to 1.50, the isentropic diffuser efficiency was 0.80 ± 0.05. This efficiency takes into account the shock losses, the friction losses, and the eddy current losses induced by the sharp change in velocity. This value is in general agreement with data from supersonic diffusers.[9] For $M > 1.25$, the method of calculation assumes an isentropic diffuser efficiency (0.8) in the present case together with conservation of energy and mass to determine the conditions behind the shock.

The equations previously described are used to calculate an effective main flow with these initial conditions calculated behind the shock. At the end of the separated region, the theoretical and experimental results are compared. This comparison leads to a verification of the isentropic efficiency that was used. Figure 9 compares the two calculations 1) of the separated boundary layer, and 2) using the isentropic diffuser efficiency for the separated region. Good agreement is found at the reattachment point.

C. Length of Separated Region

As mentioned before, the Lorenz force causes the electrode boundary layer to separate and delays its reattachment. Because of the separation, the velocity is only fully recovered at the reattachment point, and an adverse pressure gradient exists throughout the separated boundary layer. The recovery pressure is reduced by the effect of the Lorenz force acting on the mainstream. Close to the reattachment point, the streamlines will become parallel to the wall, and the transverse pressure gradient will vanish. Therefore, the momentum equation can be written as

$$(dp/dx) + JB = (\partial \tau / \partial y)_w \qquad (5)$$

in the immediate vicinity of the wall; JB is the Lorenz force, and $(\partial \tau / \partial y)$ is the Reynolds stress.

Using an analysis similar to Gadd's,[10] the boundary-layer equations developed in the Appendix indicate the existence of a point of minimum Reynolds stress (Fig. 11). Upstream of that point, the pressure gradient predominates, whereas downstream of it, the Lorenz force increases the Reynolds stress. The analysis (Fig. 11) also indicates that the minimum Reynolds stress becomes more shallow as the interaction decreases. This region of minimum Reynolds stress is the most likely for reattachment. The point of minimum stress has been chosen as the point of reattachment which is accurate for strong interaction, but less accurate as the interaction decreases. Furthermore, as the interaction decreases, the separation length increases. This effect also indicates that the reattachment is caused by the Lorenz force. For weak interaction, reattachment occurs in the diffuser, or separation remains throughout the channel. In the latter case, the channel flow may have been overexpanded slightly, and the separation region may have been influenced by the
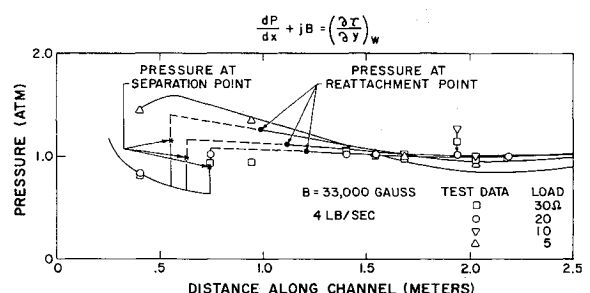

Fig. 12 Comparison of calculated pressure distribution, shock location, and length of separated boundary layer with experimental data for 4 lb/sec and 33,000 gauss.

back pressure according to empirical criteria as described in Ref. 12.

Figure 12 gives the calculated pressure distribution, the shock location, and the length of boundary layer for different load conditions at a mass flow of 4 lb/sec. The figures indicate the general good agreement. The upper curve, obtained under heavy loading, describes a fully subsonic flow, which is developed up to the first electrode and accelerated downstream of it.

IV. Electrical Boundary Layer

The loading of the generator causes an electric field to exist in the gas and the electrons to drift in the direction perpendicular to the electric and magnetic fields. In a linear generator with segmented electrodes, this Hall effect results in an axial field, as shown in Fig. 13.

The finite-length electrodes form an equipotential surface, which locally provides a zero impedance path for the Hall voltage. This local shorting of the Hall field results in a concentration of current on the downstream edge of the electron-emitting electrode and on the upstream edge of the anode.

Such an effect results in the existence of an electric boundary layer, which was calculated theoretically[2,3] and shown experimentally.[1] This local shorting of the Hall field results in local joule losses, which depend upon the magnitude of the Hall coefficient and channel geometry for given conditions.

In the series of tests under study, both the magnitude of the Hall coefficients $\omega\tau$ and the electrode geometry have been changed. The geometry change consists in a variation of the ratio of the electrode pitch to the channel height. This variation was obtained by connecting one, two, three, or four adjoined electrodes in parallel onto the same load (10Ω). (These connections are denoted 10, 20, 30, and 40.) The increased joule loss can be considered as resulting from a change in effective conductivity. Figure 14 shows the variation of the average conductivity as determined from the analysis of the tests run at 6.5 lb/sec and 33,000 gauss. Allowing for the change of $\omega\tau$ from run to run, the conductivity variation corresponds to

$$\sigma_{eff}/\sigma_0 \simeq 1/1 + \omega\tau(s/h)$$

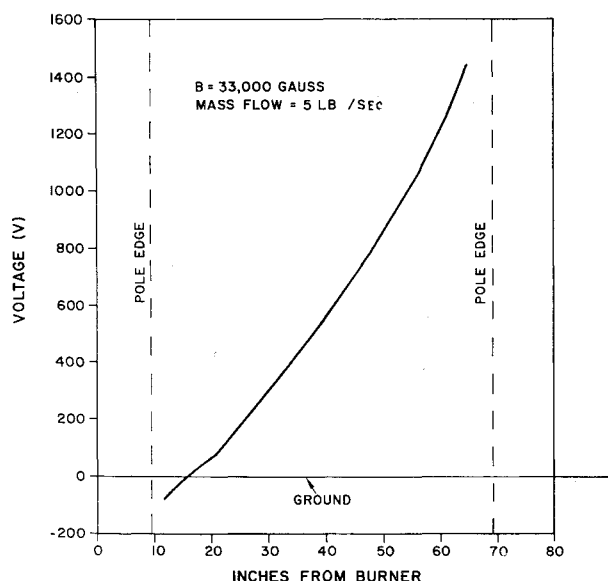where s is the electrode pitch and h the channel height, which is predicted by the analysis.[2,3]

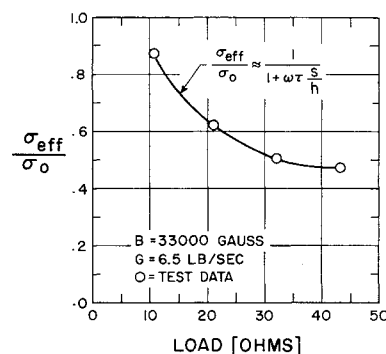Fig. 13 Distribution of Hall field in a linear generator (short-circuit conditions).

Fig. 14 Ratio of effective to scalar conductivities as a function of the electrode pitch to channel height ratio (s/h).

However, this joule loss occurs at the surface of the electrode and appears as an electrode loss, as it is considered in the detailed analysis. The magnitude of the loss is determined from the analysis by Crown,[3] who solves the current distribution without resorting to restrictive boundary conditions imposed on the axial component of current.[2] The electrode drop associated with the Hall effect can be represented by its equivalent field $E_{e1H} = (UB - E_2)(I_y - 1)$, where I_y is the correction term represented in Fig. 15, derived from the analysis. E_2 is the field in the mainstream, U is the velocity, and B is the magnetic field. With this knowledge, the electrode drop because of the Hall effect can be computed at each axial location and its influence determined. The electrode drop computed comprises the terms associated with both the aerodynamic and electrical boundary layers. Figure 16 gives the distribution of $\omega\tau$ and of the electric fields associated with the joule and electrode losses. In this run, the shock was present at the inlet. The electrode drop rises with $\omega\tau$ in the supersonic region and again at the end of the subsonic region where the flow is close to sonic. The drop in $\omega\tau$ and electrode drop at the downstream end results from the fringing of the field. The difference between the electric field in the gas and the field associated with electrode drop is equal to the calculated field applied to the load. Figure 17 displays the same result, but for a run with three electrodes in parallel onto the same loads. The field associated with electrode drop becomes comparable to the joule loss in the mainstream and reduces the performance appreciably. The effect of $\omega\tau$ on the electrode drop can be obtained by comparing results upstream and downstream of the shock. These results indicate that the use of wide electrodes has a very unfavorable influence on the generator performance. In conclusion, the ratio $\omega\tau$ s/h is to be kept much smaller than 1. The preceding figures indicate local electrical efficiency larger than 80% with an isentropic efficiency of 65%. The use of electrodes of much smaller
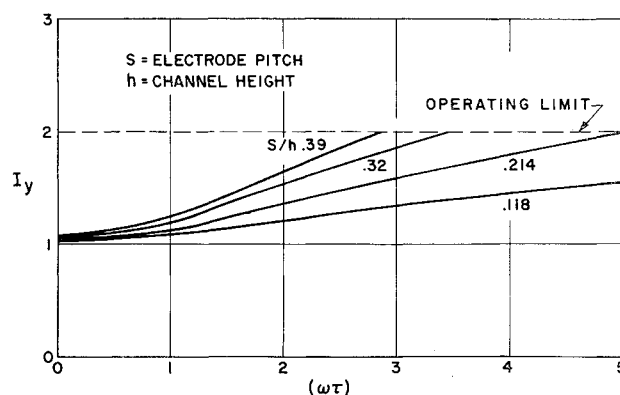
Fig. 15 Electrode loss term (I_y) as a function of the Hall coefficient and s/h.
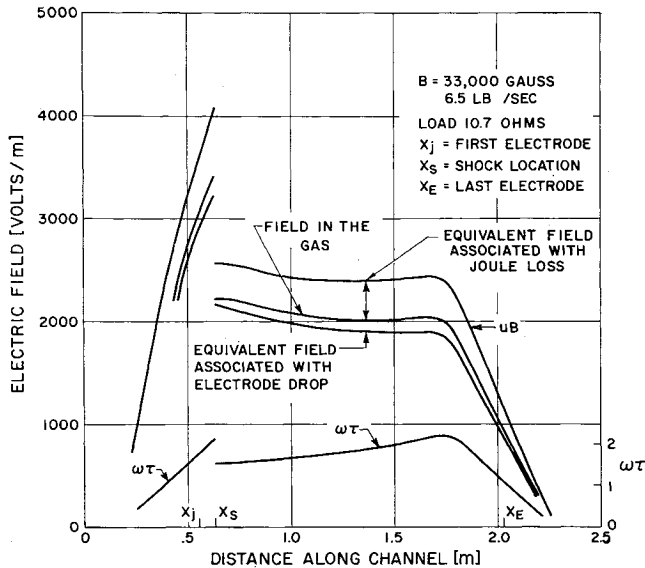
Fig. 16 Hall coefficient, electrode drop, induced, and applied fields as a function of distance (6.5 lb/sec, 10 Ω, and 33,000 gauss).

pitch would have resulted in efficiency larger than 90% (Fig. 17). For large ratio of the electrode to insulator widths, Crown indicated that a leakage current might exist between adjacent electrodes.[3] Evidence of such a leakage was found from a deterioration of the performance at $\omega\tau \simeq 2.5$ and from damage to the insulation between electrodes. This damage was found only on the negative side of the channel where the Lorenz force acting on the current drives it into the wall insulation.

The Hall effect taking place at the electrode results in the circulation of an average axial current. This component of axial current can be decreased by staggering the electrode connections,[2] i.e., one electrode is not connected through the load to the opposite electrode but to the next one or the following ones. Such tests were conducted on the channel of 1.5 area ratio at an $\omega\tau$ of 1.5. They showed that a staggering by one electrode was optimum and resulted in an over-all performance improvement from 545 to 600 kw.

V.   Channel Over-All Performance and Conclusions

The same detailed calculation of the flow was applied to each test, specifying the inlet and loading conditions only. For each test, the pressure, the power output (Fig. 18), and the voltage distribution (Fig. 19) were compared to the experimental data with a good degree of agreement. Finally, Fig. 1 compares the experimental and calculated over-all performance of the Mark II generator under widely varying conditions of mass flows and loading.

To conclude, an MHD generator has been operated over a wide variety of mass flows, pressure ratio, Hall coefficient, and electrode geometry. These experiments demonstrated that there is a gain of performance to be derived by establishing a moderately supersonic flow in an MHD generator. It further showed that, for the supersonic flows of interest $(M \leq 1.5)$, the pressure loss caused by a shock in off-design conditions is only slightly detrimental to the performance.

The quasi-one-dimensional theory used is found to describe the flow accurately and in detail. The agreement is found over a wide range of supersonic, transonic, subsonic flows, and electrode geometries. The detailed analysis used gives a good insight into the importance of losses at each axial location. The channel performance can be determined and analyzed. This analysis can be used to predict the per-

formance of MHD generators at design and off-design conditions. It can also be used to study the problems of control associated with the regulation of an MHD generator.

Finally, it has been found that the electrode losses associated with the presence of a Hall field can hamper seriously the performance of an MHD generator. Although this loss can be reduced by augmenting the degree of electrode segmentation with increasing values of the Hall field, practical engineering limits to segmentation will exist.

Appendix

Simplified Analysis for Free-Interaction Region

Separation pressure

As known from basic aerodynamics, a strong enough shock could cause separation in the boundary layer. Some of our experimental data showed evidence of this phenomena.

It is assumed that the boundary layer is wholly turbulent. Furthermore, it is not fully developed in the channel. Therefore, a flat-plate model is feasible. The configuration envisioned is as in Fig. 20. There is a very steep initial pressure rise up to the separation point 2. Downstream of 2, for some distance, there is a "dead air" air region next to the wall. The thickness of this dead air region increases rapidly downstream of point 2 until it reaches an apex. Because of the pressure gradient in the mean flow, the boundary layer will reattach at some point further downstream. The pressure asymptotes to the peak pressure P_4, which is reached shortly after the reattachment point. For conventional channel flow, the ratio of this peak pressure to the original freestream pressure is approximately the same as if there were no separation. However, for MHD flow, this ratio is less because of the Lorenz force.

From Eq. (4), it follows directly that the separation pressure is given by

$$\frac{P_2}{P_1} = \left[\frac{1 + [(\gamma - 1)/2]M_1{}^2}{1 + [1 - (u/U)^2][(\gamma - 1)/2]M_1{}^2} \right]^{\gamma/\gamma - 1} \quad (A1)$$

For our calculation, $u/U = 0.6$ is chosen which corresponds to $C = 0.64$ in Eq. (4).

Length of separated region

If a pressure distribution is determined locally by free interaction of boundary layer and external subsonic flow, then
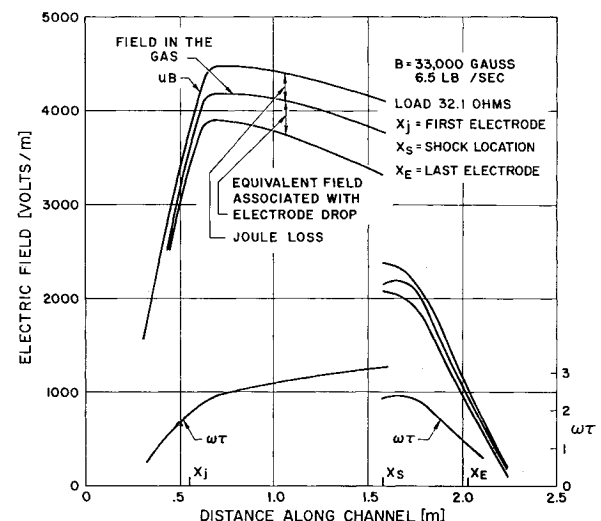

Fig. 17 Hall coefficient, electrode drop, induced, applied fields as a function of distance (6.5 lb/sec, 30 Ω, and 33,000 gauss).

the applicable equations are the momentum equation for steady flow in the viscous layer coupled with the mass continuity for the control volume. The usual boundary-layer momentum equation

$$\rho u \frac{du}{dx} + \rho v \frac{du}{dy} = F - \frac{dp}{dx} + \frac{\partial \tau}{\partial y} \quad\quad (A2)$$

would apply, provided that the transverse pressure gradient within the layer is small as compared to the streamwise gradient. At the separation point, the streamline curvature is large. Close to the point of reattachment, the curvature of the streamline is negligible, and the momentum equation reduces itself to

$$(dp/dx) - F = (\partial \tau / \partial y)_w \quad\quad (A3)$$

in the immediate vicinity of the wall. The wall shear stress τ_{w3} at the beginning of interaction will be the measure of the variable wall shear τ_w, by simply saying that $\tau_w = k\tau_{w3}$ where k is a proportionality constant. The friction stress τ_{w3} is equal to $-\rho u'v'$ so that near the wall

$$\left(\frac{\partial \tau}{\partial y} \right)_w = K \frac{\gamma M_1{}^2 P_3 u_3{}^2}{\{1 + [(\gamma - 1)/2]M_1{}^2\}u_1{}^2 \delta} \quad\quad (A4)$$

Obtaining this equation, it is assumed that the reattachment velocity is roughly linear with y. The pressure gradient at a point downstream of the shock location is roughly proportional to

$$dp/dx \approx [P(x) - P_2]/(x - x_s) \quad\quad (A5)$$

F represents body force in Eq. (A2), which is the Lorenz force in our case. It is assumed that, in the interaction region $(x - x_s)$, an average Lorenz force is applicable

$$(j \cdot B)_{\text{av}} = \frac{1}{2} \left(\left\{ B \frac{\sigma \sigma_L}{\sigma + \sigma_L} [BM(\gamma RT)^{1/2} - E_{\text{el}}] \right\}_2 + \right.$$
$$\left. \left\{ B \frac{\sigma \sigma_L}{\sigma + \sigma_L} [BM(\gamma RT)^{1/2} - E_{\text{el}}] \right\}_{x - x_s} \right)$$

Substituting Eqs. (A4) and (A5) into Eq. (A3), one obtains

$$\left. \begin{array}{l} \dfrac{P - P_2}{x - x_s} + [jB]_{\text{av}} = \\[2mm] \qquad K \dfrac{\gamma M_1{}^2 P_3}{\{1 + [(\gamma - 1)/2]M_1{}^2\}} \left(\dfrac{u_3}{u_1} \right)^2 \dfrac{1}{\delta} \\[4mm] \text{or} \\[2mm] \dfrac{\delta}{\delta_1} = \left(\dfrac{\delta_1{}^*}{\delta_1} \right) \dfrac{1}{\delta_1{}^*} \dfrac{K \dfrac{\gamma M_1{}^2 P_3}{\{1 + [(\gamma - 1)/2]M_1{}^2\}} \left(\dfrac{u_3}{u_1} \right)^2}{[P - P_2/(x - x_s)] + (jB)_{\text{av}}} \end{array} \right\} \quad (A6)$$
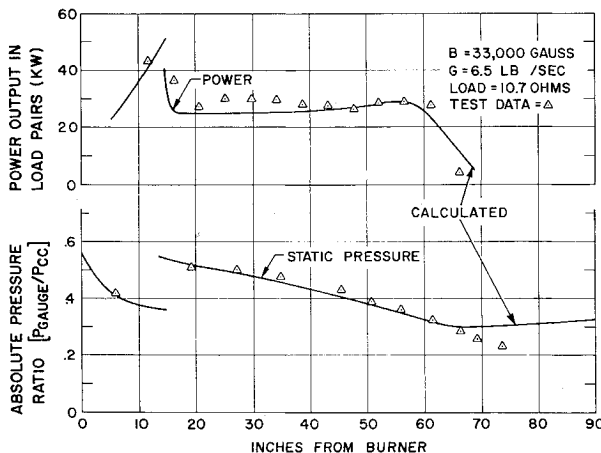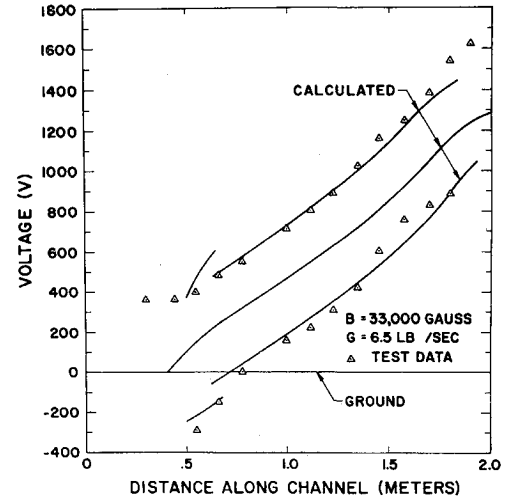

Fig. 19   Comparison of experimental and calculated voltage distribution.

Turning now to the continuity equation for the control volume shown in Fig. 20, flow across xx' − flow across $11'$ = flow across $1'x'$ since the velocity ratio includes the MHD effects. Therefore, Eq. (15) of Ref. 10 is applicable

$$q\delta - q_1\delta_1 = 0.025(\delta_2 u_2 + \delta u/2\delta_1 u_1)(x - x_s) \quad\quad (A7)$$

where

$$q_1 = 1 - (\delta_1{}^*/\delta_1)$$

$$q = \left(\frac{P}{P_1} \right) \frac{1}{(u/u_1)} \frac{1}{(\gamma_1{}^{-1}/2)M_1{}^2} \left[a \log_e \frac{a + 1}{a - 1} - 2 \right]$$

$$\left(\frac{u}{u_1} \right) = \frac{M}{M_1} \left(\frac{\gamma}{\gamma_1} \frac{R}{R_1} \frac{T}{T_1} \right)^{1/2}$$

$$a = \left[\frac{1 + [(\gamma_1 - 1)/(\gamma_1 + 1)]M_1{}^2}{(u/u_1)^2[(\gamma_1 - 1)/2]M_1{}^2} \right]^{1/2}$$

Substituting Eq. (A6) into Eq. (A7), one can attain the following result:

$$\left(\frac{\delta_1{}^*}{\delta_1} \right) \frac{1}{\delta_1{}^*} \left\{ q \frac{K\{\gamma M_1{}^2 P_3/[1 + [(\gamma_1 - 1)/2]M_1{}^2]\}(u_3/u_1)^2}{[P - P_2/(x - x_s)] + [jB]_{\text{av}}} - \right.$$
$$\left. 0.025 \left[\left(\frac{\rho_2}{\rho_1} \right) \left(\frac{u_2}{u_1} \right) \right] (x - x_s) \right\} - q_1 \quad (A8)$$

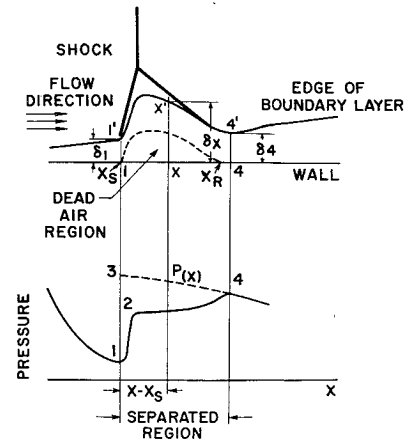$(\delta_1{}^*/\delta_1)$, as a function of M_1, is given in Table 1. $\delta_1{}^*$ is ap-

Fig. 18   Comparison of experimental and calculated distribution of pressure and power output.

Fig. 20   Schematic flow field close to a shock wave and the associated separated boundary layer.

Table 1

M_1	$\delta_1{}^*/\delta_1$
0	0.13
1	0.16
2	0.24
3	0.33

proximately given by Ref. 11 for a zero pressure gradient boundary layer.

$$\delta_1{}^* = \frac{0.0475(1 + 0.35M_1{}^2)x_1}{[1 + 0.88[(\gamma - 1)/2]M_1{}^2]^{0.44} (Gx_1/A_1\mu_1)^{0.2}} \quad (A9)$$

References

[1] Louis, J. F., Lothrop, J., and Brogan, T. R., "Fluid dynamic studies with a magnetohydrodynamic generator," Phys. Fluids 7, 362 (1964).

[2] Hurwitz, H., Kilb, L. W., and Sutton, G. W., "Influence of tensor conductivity on current distribution in a MHD generator," J. Appl. Phys. 32, 205 (1961).

[3] Crown, J. C., "Analysis of magneto gas dynamic generators having segmented electrodes and anisotropic conductivity," United Aircraft Rept. R 1852-2 (February 1961).

[4] Teare, J. D., "Thermodynamic equilibrium calculations for carbon-hydrogen-oxygen-nitrogen mixtures," Avco-Everett Research Lab. Rept. AMP 104 (May 1961).

[5] Louis, J. F. and Decher, R., "MHD generator performance under non-uniform and time varying load," Avco-Everett Research Lab. Research Rept. 148 (March 1963).

[6] Kantrowitz, A. R., "One-dimensional treatment of non-steady gas dynamics," Fundamentals of Gas Dynamics, edited by H. W. Emmons (Princeton University Press, Princeton, N. J., 1958).

[7] Mager, A., "Prediction of shock-induced turbulent boundary-layer separation," J. Aeronaut. Sci. 22, 201 (1955).

[8] Schuh, H., "On determining turbulent boundary-layer separation in incompressible and compressible flow," J. Aeronaut. Sci. 22, 343 (1955).

[9] Crocco, L., "One-dimensional treatment of steady gas dynamics," Fundamentals of Gas Dynamics, edited by H. W. Emmons (Princeton University Press, Princeton, N.J., 1958).

[10] Gadd, G. E., "Interactions between wholly laminar or wholly turbulent boundary layers and shock waves strong enough to cause separation," J. Aeronaut. Sci. 20, 729 (1953).

[11] Monaghan, R. J., "Comparison between experimental measurement and suggested formula for the variation of turbulent skin friction in compressible flow," Great Britain Aeronautical Research Council TR C. P. 45 (1950).

[12] Arens, M. and Spiegler, E., "Shock-induced boundary layer separation in overexpanded conical exhaust nozzles," AIAA J. 1, 578–581 (1963).

Generation and Characteristics of Plasma Wind-Tunnel Streams

DAVID F. HALL,* ROBERT F. KEMP,* AND J. M. SELLEN JR.*

TRW Space Technology Laboratories, Redondo Beach, Calif.

The plasma wind tunnel permits the laboratory study of the interaction of a moving material body with a dilute plasma, such as the ionosphere, and the laboratory calibration of spacecraft plasma diagnostic instrumentation. Plasma streams, with uniform density cross sections ~30 cm diam of H_2, He, N_2, O_2, Ne, A, CO_2, and Cs, and some mixtures thereof, have been produced at 1.6 m from an 11-cm electron bombardment and a 2.5-cm contact ion source. Except for H_2 and He, velocities and densities appropriate for simulation of a satellite in circular orbit below the heliosphere (≤ 8 km/sec, $\leq 10^6$ ions/cm^3) are included in the range of operation of these sources. The ion velocity spread in the longitudinal direction, encountered by a satellite, caused by the ion thermal motion has been simulated through the variation of plasma source accelerating potential. Simulation of transverse velocity components caused by thermal motion has been achieved through the use of electrostatic scattering fields imposed on the stream.

Nomenclature

v_+	=	ion velocity, km/sec
j_+	=	ion current density, amp/cm^2
V	=	potential, v
$\tilde{V}$	=	maximum value of perturbation potential, v
q	=	electric charge, coul
ΔW	=	width of energy distribution, ev
N	=	total number of particles in system
n	=	plasma density, ions/cm^3
k	=	Boltzmann's constant, 1.38×10^{-23} joules/°K
T	=	Kelvin temperature
M	=	mass, kg
r	=	radius, radial distance, cm
Λ	=	klystron bunching length, cm
L	=	axial length of the divergence analyzer, cm
l	=	source to object distance, cm
θ	=	maximum beam divergence angle of uniform portion

Subscripts

$+$	=	ion
d	=	deflection
e	=	electron
s	=	spacecraft
p	=	plasma
pr	=	probe
0	=	average beam value
1	=	perturbation value
is	=	ion source
th	=	average thermal